AGU Advances

Supporting Information for:

Slow slip events and megathrust coupling changes reveal the earthquake potential before the 2020 Mw 7.4 Huatulco, Mexico event

Authors: Carlos Villafuerte[1]*, V. M. Cruz-Atienza[2], J. Tago[3], D. Solano-Rojas[3], R. Garza-Girón[4], S. I. Franco[2], L. A. Dominguez[5] and V. Kostoglodov[2].

[1]Posgrado en Ciencias de la Tierra, Instituto de Geofísica, Universidad Nacional Autónoma de México, Mexico City, Mexico.

[2]Instituto de Geofísica, Universidad Nacional Autónoma de México, Mexico City, Mexico.

[3]Facultad de Ingeniería, Universidad Nacional Autónoma de México, Mexico City, Mexico.

[4]Department of Earth and Planetary Sciences, University of California, Santa Cruz, USA.

[5]Escuela Nacional de Estudios Superiores, Campus Morelia, Universidad Nacional Autónoma de México, Mexico.

*Correspondence to: villafuerte.cd@gmail.com

Contents of this file:

Text S1. GNSS time series processing

The GNSS displacement times series are estimated using the GIPSY 6.4 software package (Lagler et al., 2013), which follows a Precise Point Positioning strategy. The station positions are defined in the International Terrestrial Reference Frame, year 2014 (ITRF 2014). For daily processing we used the Jet Propulsion Laboratory final and non-fiducial products (orbits and clocks). We generated observables using 2 model categories: (1) Earth models and (2) observation models. The Earth models include tidal effects (i.e., solid tides, ocean loading and tide created by polar motion), Earth rotation (UT1), polar motion, nutation and precession. Observation models, on the other hand, are related with phase center offsets, tropospheric effects and timing errors (i.e., relativistic effects). The troposphere delay is estimated like as random walk process. This effect is broken into wet and dry components. The azimuthal gradient and the dry component are estimated using GPT2 model and mapping function (TGIPSY1). The antennas phase center variations are considered through antenna calibration files. For receiver antennas, the correction is estimated taking the International GNSS Service (IGS) Antex file. We also applied a wide-lane phase bias to account for the ambiguity resolution.

To remove the outliers and then estimate the displacement vectors per time window, we first determine the data variance for each component and time window from the differences between daily displacement values and a moving, locally weighted LOESS function (i.e., 2nd order polynomial regressions with a half-window time support, Figs. 2a, 3a and S6). Then, all data points in a time window with differences larger than two standard deviations were

dismissed. Once the outliers are removed, a new regression is performed to estimate the final displacement vectors.

1.1 Correction of seasonal effects

To properly associate the displacement time series with the deformation produced by slip processes on the plate interface its necessary to identify and remove the signals associated with seasonal oscillations. We assume that these signals can be modeled as a linear combination of two annual and two semi-annual trigonometric terms excluding inter-annual variations (Bevis and Brown, 2014):

$$S(t_i) = b_1 \sin(2\pi t_i) + b_2 \cos(2\pi t_i) + c_1 \sin(4\pi t_i) + c_2 \cos(4\pi t_i)\,, \quad (1)$$

where $S(t_i)$ is the seasonal displacement at time t_i in years units, b_1 and b_2 are the coefficients for the annual terms and c_1 and c_2 the coefficients for the semi-annual terms. We use only inter-SSE time windows of the actual data to identify the contribution of these periodic oscillations to the observed displacements. Thus, we assume that the GNSS time series during an inter-SSE window can be modeled as the sum of their secular inter-SSE displacement and the seasonal contributions as:

$$U(t_i) = a + vt_i + S(t_i)$$

where $U(t_i)$ represents the GNSS displacement at time t_i in years units, a is the intercept and v the constant secular velocity in the inter-SSE periods. Removing the seasonal

contribution in Oaxaca is challenging because the amplitude and recurrence of the annual and semi-annual terms are comparable to those of the SSEs in the region (from 1-2 years). Since the seasonal effects are much stronger in the vertical component than in the horizontal components, we first determined the coefficients of equation 1 for the vertical component by means of a simple least squares approach. In many stations the length of the inter-SSE windows is no longer than one year, preventing a reliable seasonal-noise characterization in such restrictive time windows. To overcome this problem, we use as many inter-SSE windows as possible in the longest GNSS time series available per station to obtain both the four coefficients of the seasonal function (i.e., the same coefficients for all inter-SSE windows) and the individual secular contribution per window. The inter-SSE windows were manually selected by excluding those periods where clear SSEs and earthquakes afterslip were present (Fig. S7). Then, the displacement time series for the vertical component during inter-SSE periods can be expressed as

$$U_v(t_i) = \begin{cases} a_1 + v_1 t_i + S_v(t_i) \;\; if \;\; T_1^l < t_i < T_1^u \\ a_2 + v_2 t_i + S_v(t_i) \;\; if \;\; T_2^l < t_i < T_2^u \\ \vdots \\ a_k + v_k t_i + S_v(t_i) \;\; if \;\; T_k^l < t_i < T_k^u \end{cases}$$

where a_k and v_k are the intercept and the constant secular velocity during the k inter-SSE window, respectively, S_v is the seasonal function for the vertical component, and $[T_k^l, T_k^u]$ are the lower- and upper-time limits of the k inter-SSE window. For the treatment of the horizontal displacement components, where the amplitude of the seasonal noise is usually smaller than that of the transient tectonic deformations, we assumed that the seasonal effects on the three components are all proportional. This is a reasonable hypothesis since most of

these contributions are related to the earth's elastic response due to hydrological processes occurring on the surface (Heki et al., 2020). Therefore, the displacement for every horizontal component in the inter-SSE periods, U_h, can be represented as

$$U_h(t_i) = \begin{cases} a_1 + v_1 t_i + \alpha_h S_v(t_i) \;\; if \;\; T_1^l < t_i < T_1^u \\ a_2 + v_2 t_i + \alpha_h S_v(t_i) \;\; if \;\; T_2^l < t_i < T_2^u \\ \vdots \\ a_k + v_k t_i + \alpha_h S_v(t_i) \;\; if \;\; T_k^l < t_i < T_k^u \end{cases}$$

where α_h is the proportionality factor determined also by means of the multi-window least square method, and h stands for the north-south or east-west component. We decided to proceed in this way because when determining the seasonal functions independently per component (i.e., by independently applying the procedure described for vertical displacements to all components) we realized that the horizontal SSE signals (consistently found at several stations) were in some cases eliminated by applying the correction. Several examples illustrating our approach are shown in Figure S7.

Text S2. InSAR images processing

We calculate a coseismic interferogram of the Huatulco Earthquake using two single look complex Synthetic Aperture Radar (SAR) scenes acquired by the Sentinel-1 satellites in the Interferometric Wide Swath acquisition mode, ascending pass, track 107 (Fig. S2a). The selected scenes were acquired on June 19th and June 25th, 2020, which correspond to the pair with the shortest-possible acquisition span (6 days). The pass and track were selected to provide the best-possible coverage of the coseismic signal. We use the processing chain provided in the InSAR Scientific Computing Environment (ISCE) (Rosen et al., 2012) to

calculate the interferometric phase between the two SAR scenes, which includes a coarse coregistration assisted by a digital elevation model (DEM), a coarse inteferogram calculation, a fine coregistration, a fine inteferogram calculation, and basic phase corrections. Accordingly, we additionally use a 1 arc-second DEM from the Shuttle Radar Topography Mission (Farr et al., 2007) to complete the interferogram formation and topographic phase correction. Subsequently, we filter the interferometric phase using a Goldstein filter (Goldstein & Werner, 1998) to later perform phase unwrapping using SNAPHU (Chen & Zebker, 2000). We finally geocode the unwrapped interferogram, convert it to displacement in meters in line of sight (LOS) geometry and mask out water bodies and areas with spatial coherence lower than 0.4 (Fig. S2b).

Geodetic measurements from GNSS and InSAR have different reference frames, which requires converting one into the other to make a fair comparison of the displacements obtained by each technique. GNSS measurements are referenced in East, North and Up components, whereas satellite InSAR have a pixel-wise reference frame in terms of incidence (θ) and azimuth (α) angles, which vary pixel by pixel and define the relative LOS direction towards the SAR satellite. GNSS displacements can be projected onto the satellite's LOS direction following the expression (Hanssen, 2001):

$$GPS_{LOS} = -\sin\left(\alpha - \frac{3\pi}{2}\right)\sin\theta d_e - \cos\left(\alpha - \frac{3\pi}{2}\right)\sin\theta d_n + \cos\theta d_u$$

where GPS_{LOS} is the projection of the GNSS displacement vector onto the LOS vector, and d_e, d_n and d_u are the GNSS displacement components in the East, North and Up directions,

respectively. Based on this transformation we adapted the ELADIN inversion method (see next section) so that the Somigliana tensor used to generate the synthetic displacements was projected into the individual LOS unit vectors per InSAR data point to perform the simultaneous GNSS and InSAR data inversion.

Text S3. Slip inversion method.

The ELADIN (ELastostatic ADjoint INversion) method (Tago et al., 2021) solves a constrained optimization problem based on the adjoint elastostatic equations with Tikhonov regularization terms, a von Karman autocorrelation function and a gradient projection method to guarantee physically-consistent slip restrictions. The method simultaneously determines the distribution of PIC and relaxing slip (i.e., SSEs and afterslip) in the plate interface to explain the surface displacements. Its precision matrix, which corresponds to the inverse of the data variance matrix (see Section 1), allows to minimize the effect of data errors (i.e., cumulative processing errors and non-tectonic physical signals) by weighting the observations. For the pre-seismic and post-seismic GNSS inversions (Figs. 2 and 3), the weights are directly based on the data variance matrix per time window and displacement component (i.e., ellipses around the tips of the horizontal displacement vectors in Figures 2 and 3) (Tago et al., 2021).

For the coseismic analysis, where GNSS and InSAR displacements are simultaneously inverted (Figs. 1 and S3c), we first inverted each data set independently. The solution using only GNSS data (Fig. S3a) describes a very simple and concentrated slip patch downdip the hypocenter with a maximum value of 4.2 m and a marginally lower than expected moment magnitude Mw 7.32 with average GNSS data error of 0.2 ± 0.2 cm (Fig. S3a). The resulting

model using only InSAR data (Fig. S3b) describes a more heterogeneous slip distribution with maximum value of 2.5 m and a slightly higher moment magnitude of 7.34 with average InSAR data error of 0.0 ± 1.2 cm (Fig. S3b). To combine both data sets in a single joint inversion, the data weights were determined by trial and error until reaching a satisfactory slip solution (Fig. S3c), with maximum value of 3.4 m and average GNSS and InSAR data errors of 1.2 ± 1.0 cm and 0.2 ± 2.1cm, respectively. The optimal set of weighting factors are such that all InSAR data (i.e., the 221 LOS displacements, Figs. 1b and S2c) were attributed a value equal to one, while the GNSS data (i.e., 12 displacement components) were attributed according to the epicentral distance of each station as follows. The HUAT and OXUM sites weighed 25, the TNSJ site weighed 15, and the OXPE site weighed 5, with these values being the same in all three components per site.

In these inversions we assumed a von Karman Hurst exponent of 0.75 and restricted the slip component perpendicular to the plate convergence direction to be smaller than 0.6 m (for details see Tago et al., 2021). To determine the optimal von Karman correlation length L for the coseismic joint inversion, we analyzed the problem resolution by means of several mobile checkerboards (MOC) tests (Tago et al., 2021) for a patch size of 20 km and 2.4 m of slip. Each MOC resolution test implies 64 independent checkerboard inversions. For each test we assumed a different L ranging between 5 and 15 km. Figure S4 shows the MOC test results for the optimal correlation length L = 7 km, which maximizes the average restitution index (ARI) in the 2020 Huatulco earthquake rupture zone and minimizes the data error. An example of a checkerboard inversion with such parameterization is also show in the figure. Our optimal model parameterization guarantees that the coseismic slip inversion has a

nominal error smaller than 35% (i.e., with restitution indexes higher than 0.65) over most of the recovered rupture area for slip patches with characteristic lengths greater than or equal to 20 km (Fig. S4).

Following Tago et al. (2021) and Cruz-Atienza et al. (2021), to guarantee slip restitution indexes higher than 0.5 in the whole Oaxaca region for slip patch sizes larger than 80 km (Fig. S8), we assumed also a Hurst exponent of 0.75 and the optimal correlation length (L) of 40 km (parameters of the von Karman function controlling the inverse-problem regularization) for the pre- and post-seismic slip inversions. Also following these works, the slip rake angle could only vary 30^o with respect to the plate convergence direction.

As for the inversion exercise mentioned in the main text with a 3.5 km shallower plate interface to match the relocated hypocentral depth of 17.2 km, the slip model (Fig. S5) significantly improved the data fit (i.e., average errors of 0.7 ± 0.6 cm and 0.1 ± 1.4 cm for GNSS and InSAR data, respectively) while reproducing similar source characteristics to those of our preferred solution (Figs. 1a and S3c). However, it is worth noting some differences: (1) the maximum slip is significantly larger (4.3 m), (2) the moment magnitude is smaller (Mw 7.3) as determined from the 1 m slip contour, and (3) the rupture is more concentrated in the main patch north of the hypocenter, between 18 and 30 km deep. For consistency throughout the manuscript (i.e., to assume the same interface geometry in all presented exercises), we keep the deeper solution shown in Figure 1 for subsequent analysis.

Text S4. Coulomb Failure Stress estimation

The total static stress change on the plate interface is the sum of the stress contributions from plate interface regions that slip, producing either a stress relaxation of the continental crust (i.e., due to SSEs, coseismic slip and afterslip) or a stress built-up (due to regions in coupling regime that we modeled as backslip (Savage, 1983)). To estimate the stress tensor, following Cruz-Atienza et al. (2021) we discretized the 3D plate interface into triangular subfaults and used the artefact-free triangular dislocation method introduced by Nikkhoo and Walter (2015) for a half-space to compute the Coulomb Failure Stress change (ΔCFS) on the plate interface by assuming a locally-consistent thrust mechanism, so that:

$$\Delta CFS = \Delta\tau + \mu\Delta\sigma_n,$$

where $\Delta\tau$ represents the change of the shear stress in the direction of the fault slip (assumed to be parallel to the plate convergence direction following DeMets et al. (2010)); $\Delta\sigma_n$ is the change of the fault normal stress (positive for tension); and μ is the apparent coefficient of friction assumed to be 0.5.

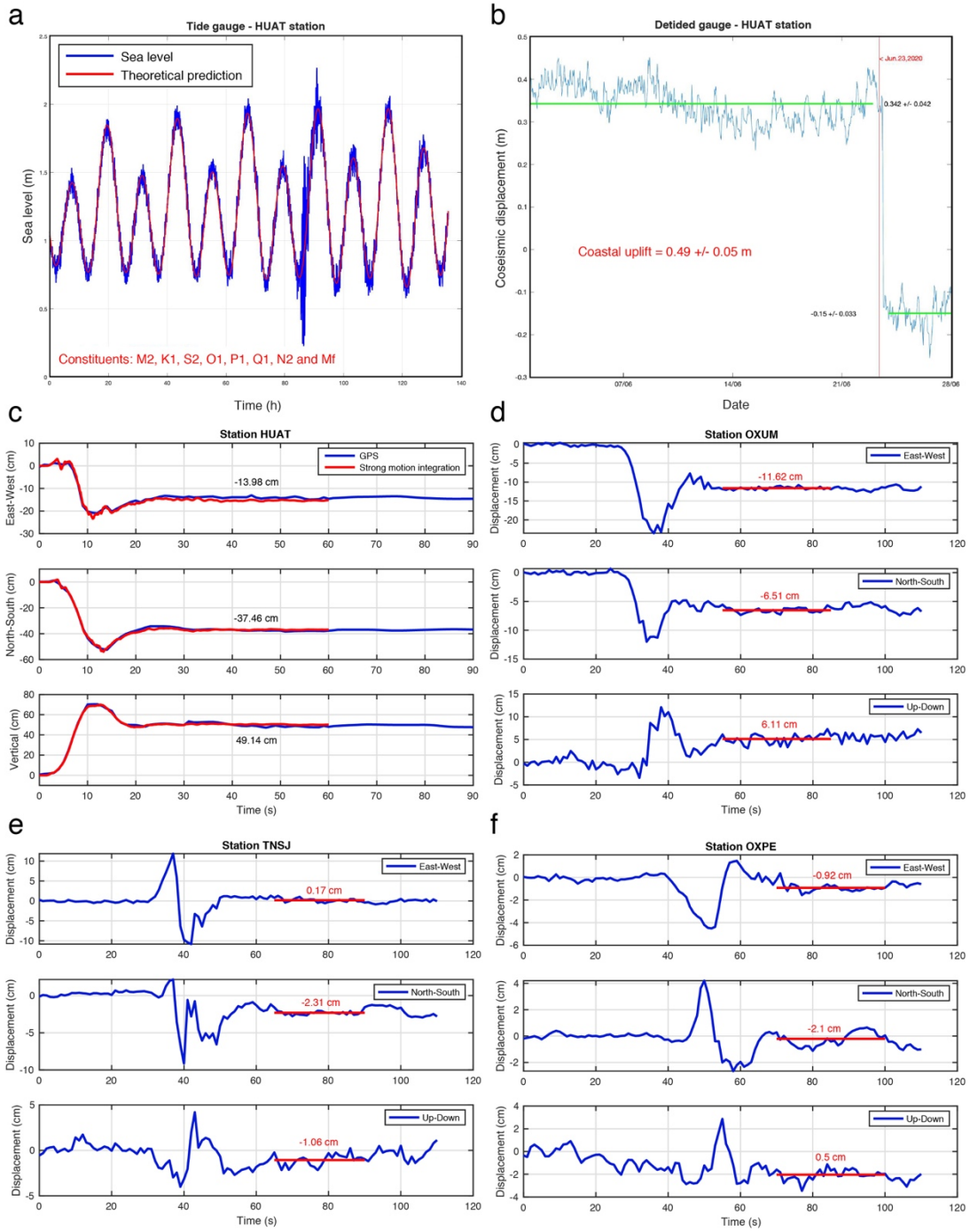

Figure S1 Huatulco earthquake co-seismic displacements estimated from the HUAT tide gauge (**a** and **b**); high-rate GNSS time series at stations HUAT (**c**), OXUM (**d**), TNSJ (**e**) and OXPE (**f**); and double integration of a strong motion record following the procedure of Wang et al. (2011)(red curve in **c**).

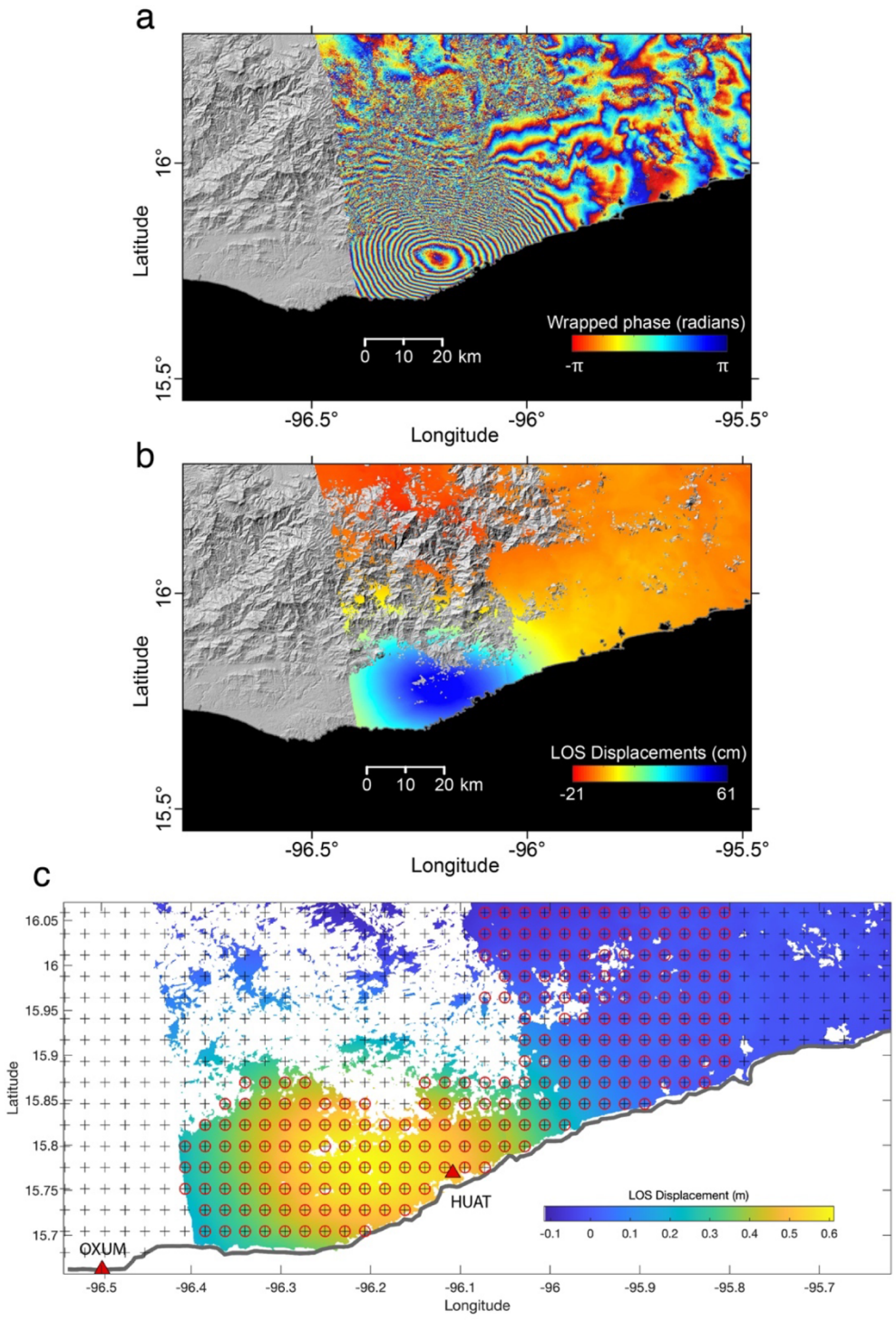

Figure S2 Huatulco earthquake InSAR displacements estimated from Sentinel satellite images on Track 107 Ascending for scenes on June 19 and 25, 2020. **a** Wrapped phase ascending interferogram. **b** Line of sight (LOS) displacement from ascending track, positive values correspond to motion towards the satellite. **c** Same than **b** but showing the data (circles with crosses) used for the coseismic inversion.

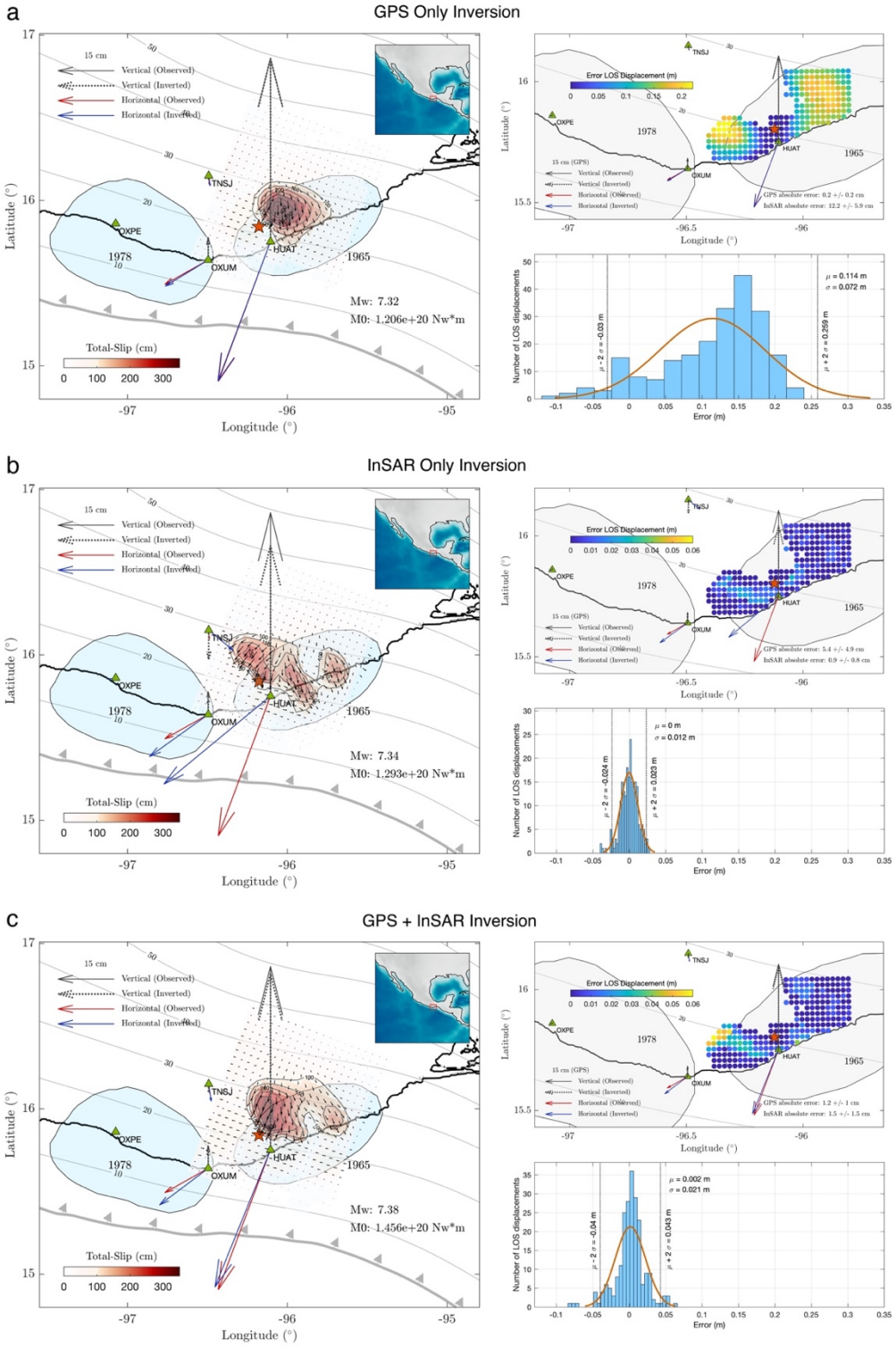

Figure S3 Coseismic slip inversions for the Huatulco earthquake using different data sets. Coseismic slip inversion (left panel) and their associated misfit GNSS and LOS displacements errors (right panels) using **(a)** only GNSS data, **(b)** only InSAR data and **(c)** both GNSS and InSAR data.

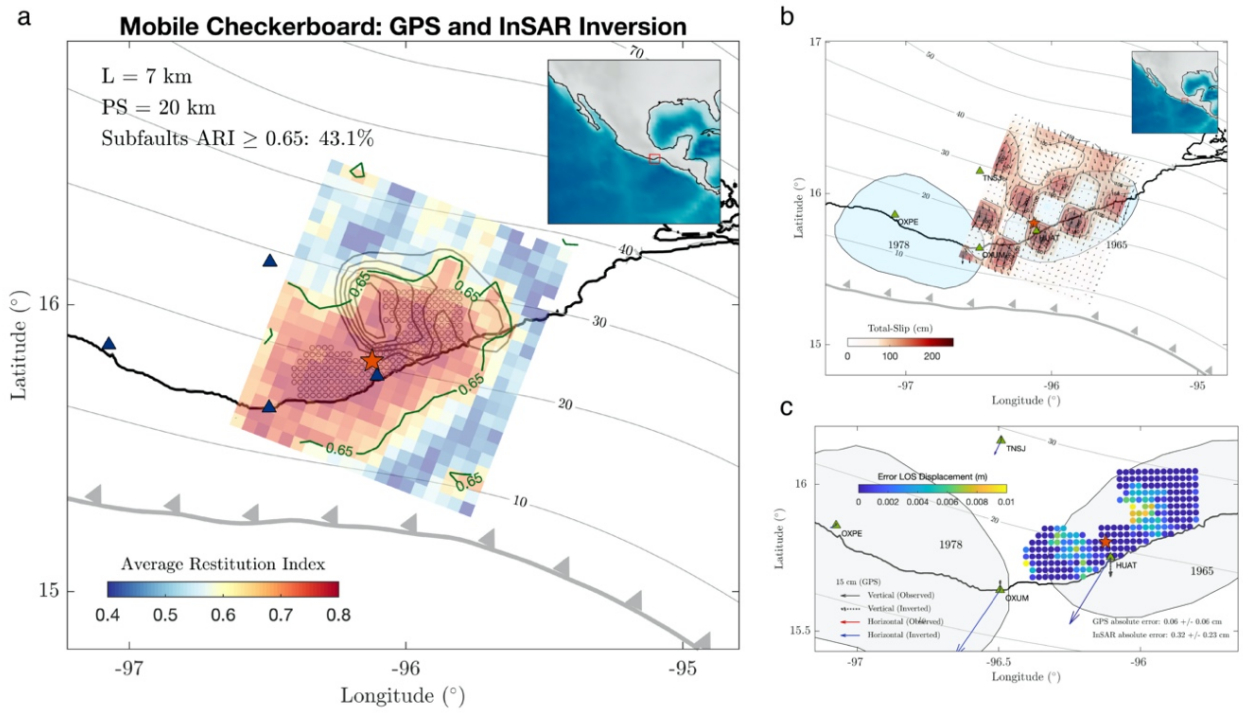

Figure S4 Resolution analysis for the coseismic GNSS+InSAR joint inversion. **a** Average restitution index (ARI) obtained from a mobile checkerboard (MOC) analysis that integrates 64 independent checkerboard inversions with patch size (PS) of 20 km and correlation length (L) of 7 km. Blue triangles are the GNSS stations, small gray circles the InSAR data sites, gray contours our preferred slip model for the 2020 Huatulco earthquake and the red star its epicenter. **b** Example of a single checkerboard slip inversion of the MOC test. **c)** GNSS and InSAR displacement errors associated with the checkerboard test shown in **b**.

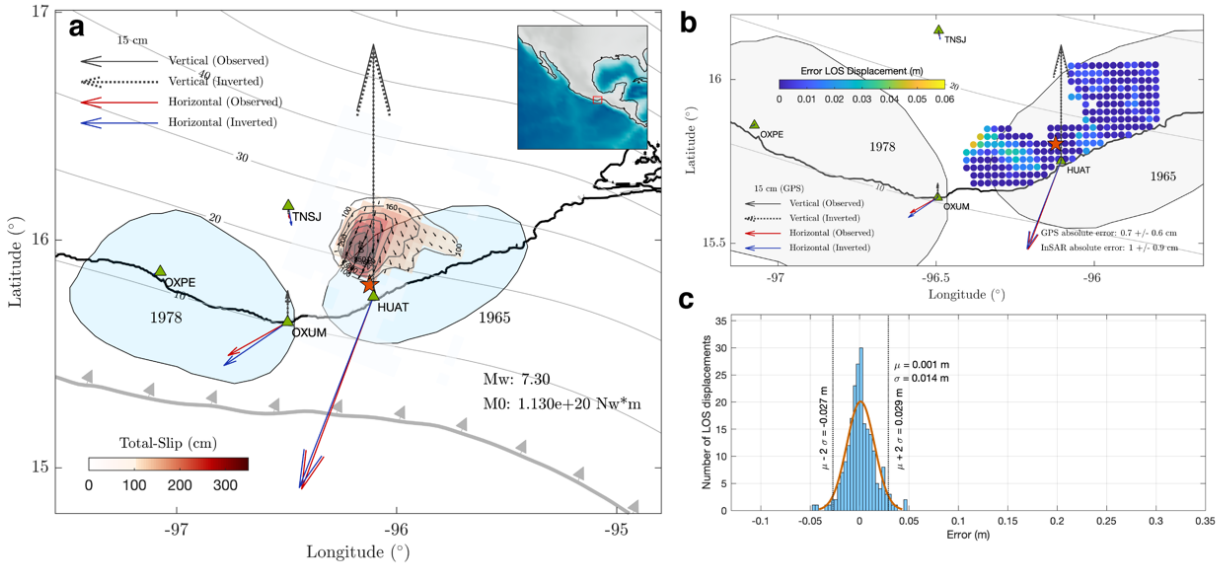

Figure S5 Huatulco earthquake joint inversion (GNSS and InSAR) assuming that the plate interface has a depth of 17.2 km at the epicenter (i.e., shifted ~3.5 km upwards with respect to the interface shown in Figure S3). Coseismic slip inversion (**a**) and their associated misfit GNSS and LOS displacements errors (**b** and **c**).

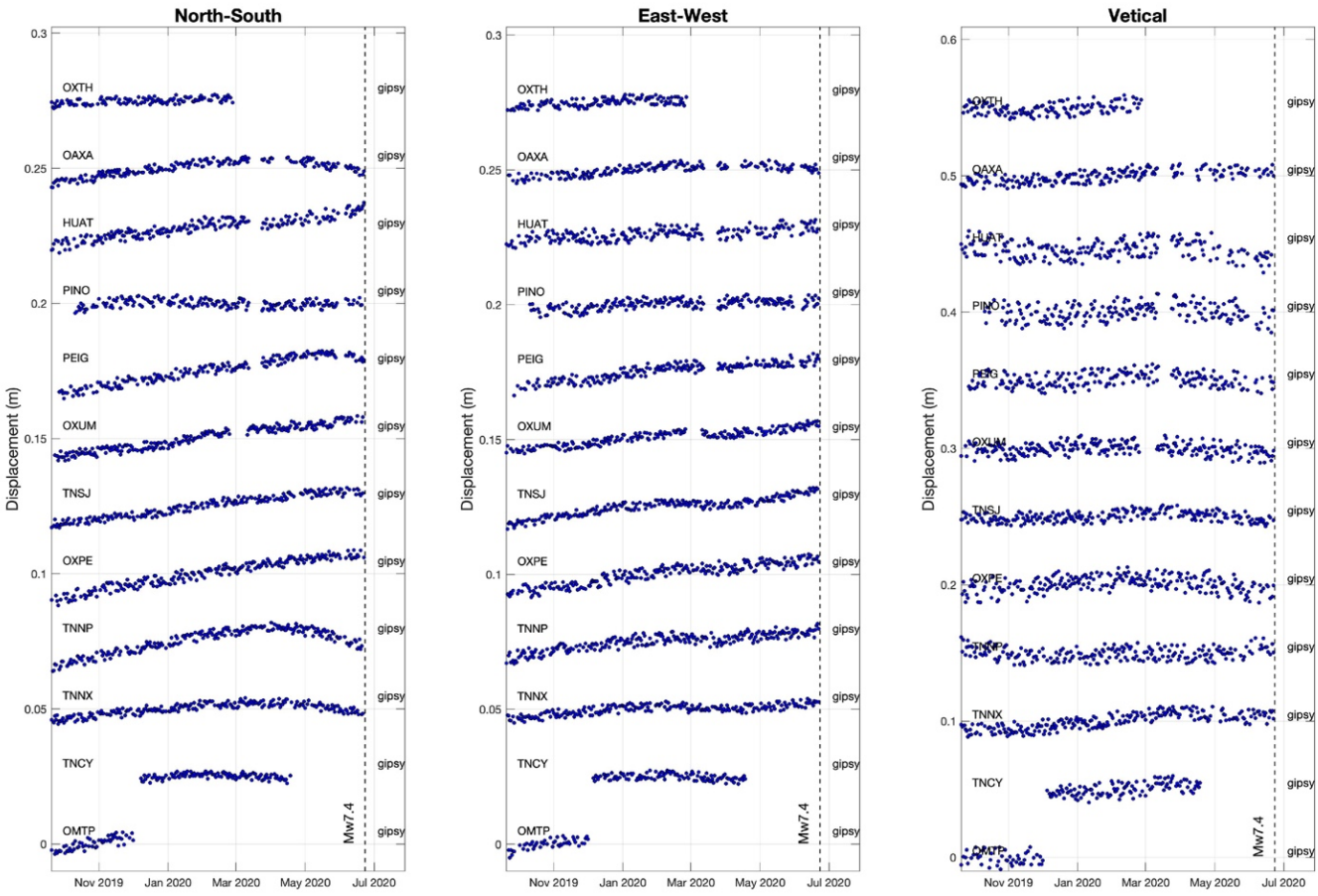

Figure S6 GNSS displacement time series estimated with the Gipsy-Oasis (v6.4) software for the pre-seismic period in the 12 stations and the three components.

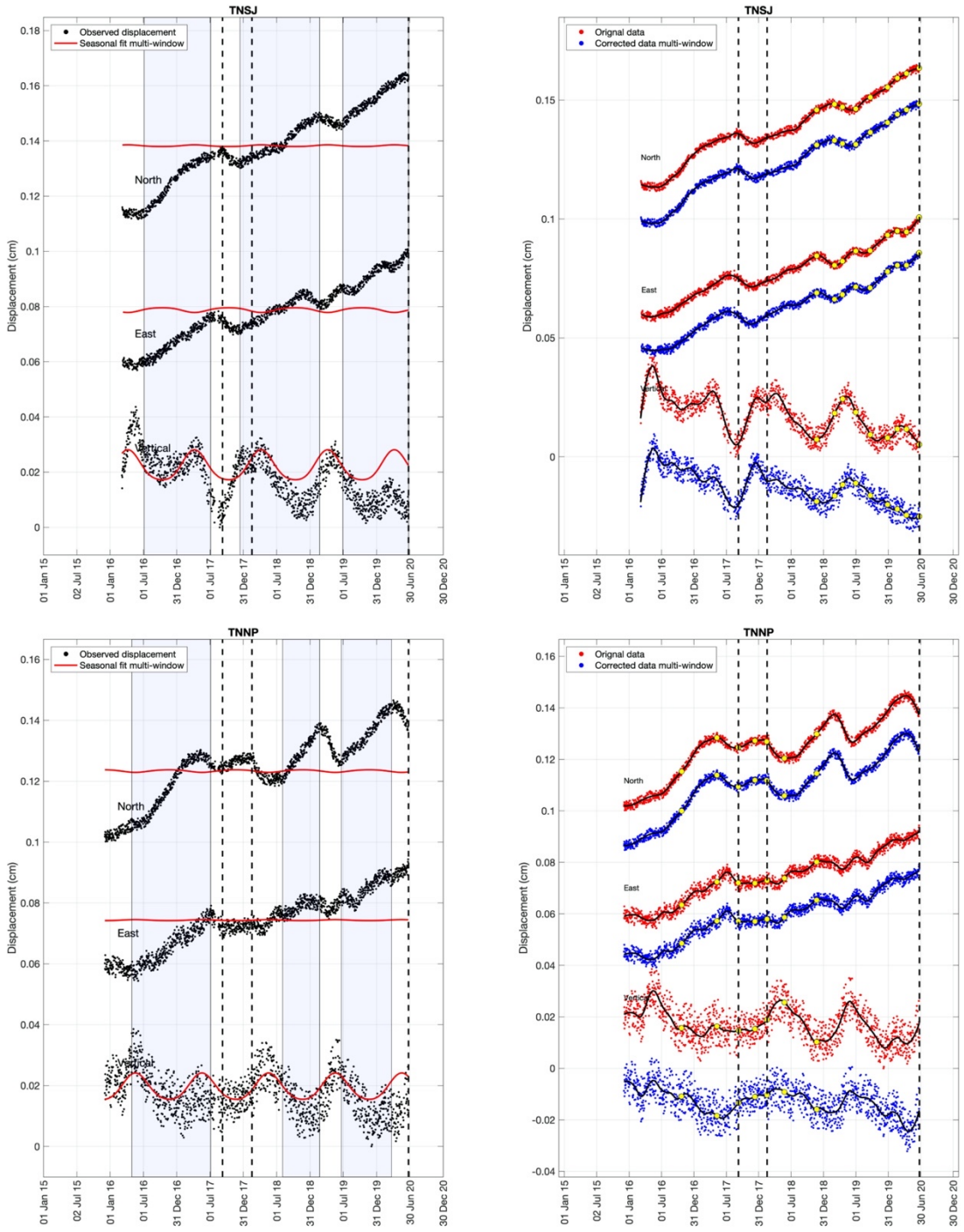

Figure S7 Example of the correction of displacement time series in station TNSJ for seasonal effects. **a** Pre-processed GNSS time series (black dots) and seasonal functions for every component (red curves) estimated from the multi-window fit procedure. **b** Original (red dots) and corrected (blue dots) displacement time series.

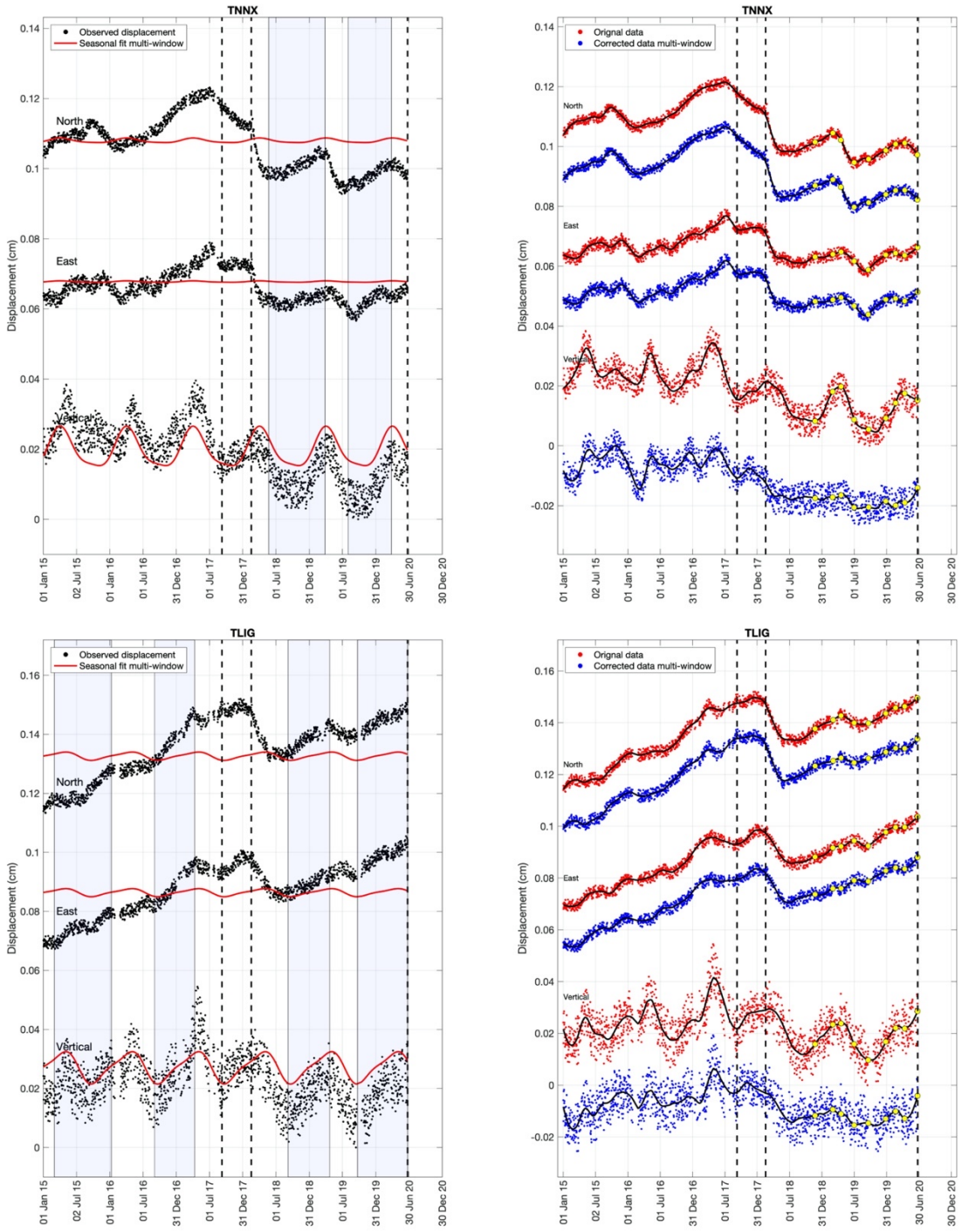

Figure S7 Continuation.

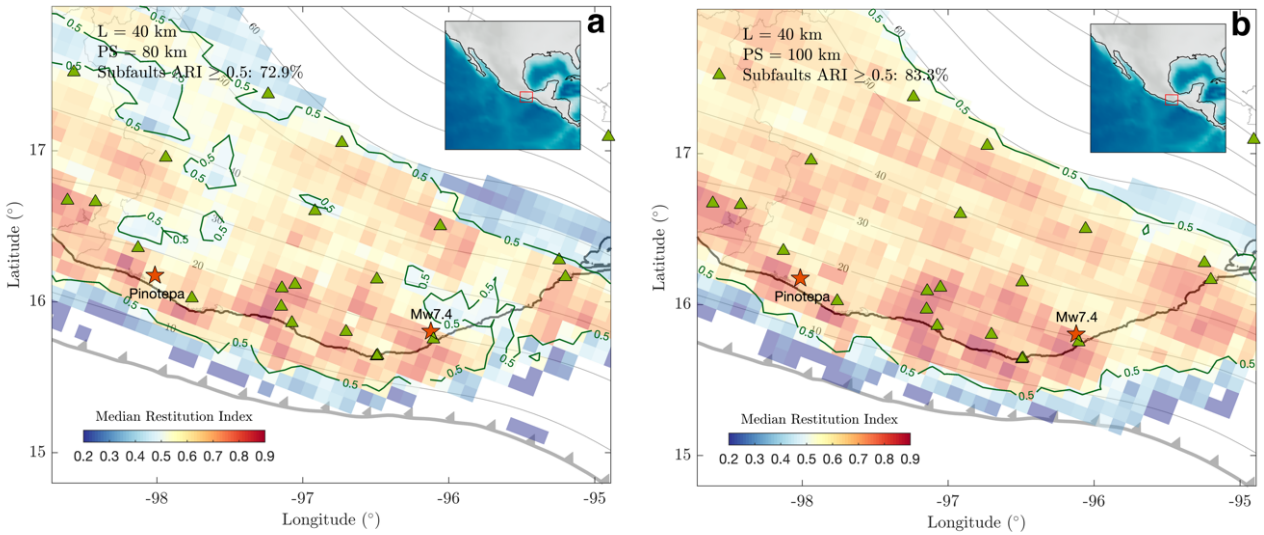

Figure S8 Resolution analysis for the aseismic slip inversions in Oaxaca. **a** Distribution of the median restitution index obtained from the mobile checkerboard inversion tests considering slip patches sizes of 80 km. **b** Same than a but with slip patches sizes of 100 km. Notice how well resolved are the plate interface regions with depths greater than 10 km.

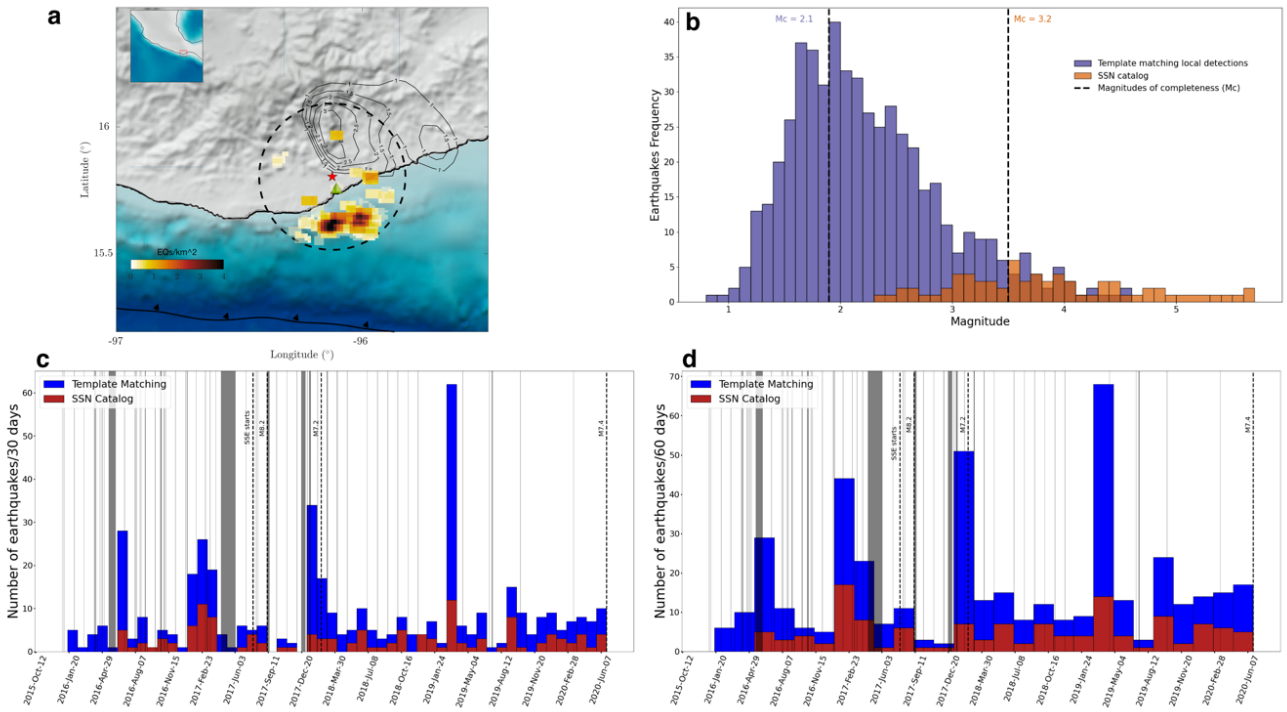

Figure S9 Illustration of template matching (TM) results using the one station method (Cruz-Atienza et al., 2020). **a** Density map of precursor TM detections using the closest station HUIG (green triangle) within 30 km from the Huatulco earthquake hypocenter (red star) and M > 2.1. Notice how almost all the detections are concentrated updip of the hypocenter due to the scarcity of templates located in the Huatulco rupture area. **b** Frequency distributions for the TM and SSN catalogs and their associated magnitude of completeness. **c**,**d** Seismicity rate evolution for the TM and SSN for two different earthquake rates. Gray sections indicate data gaps.

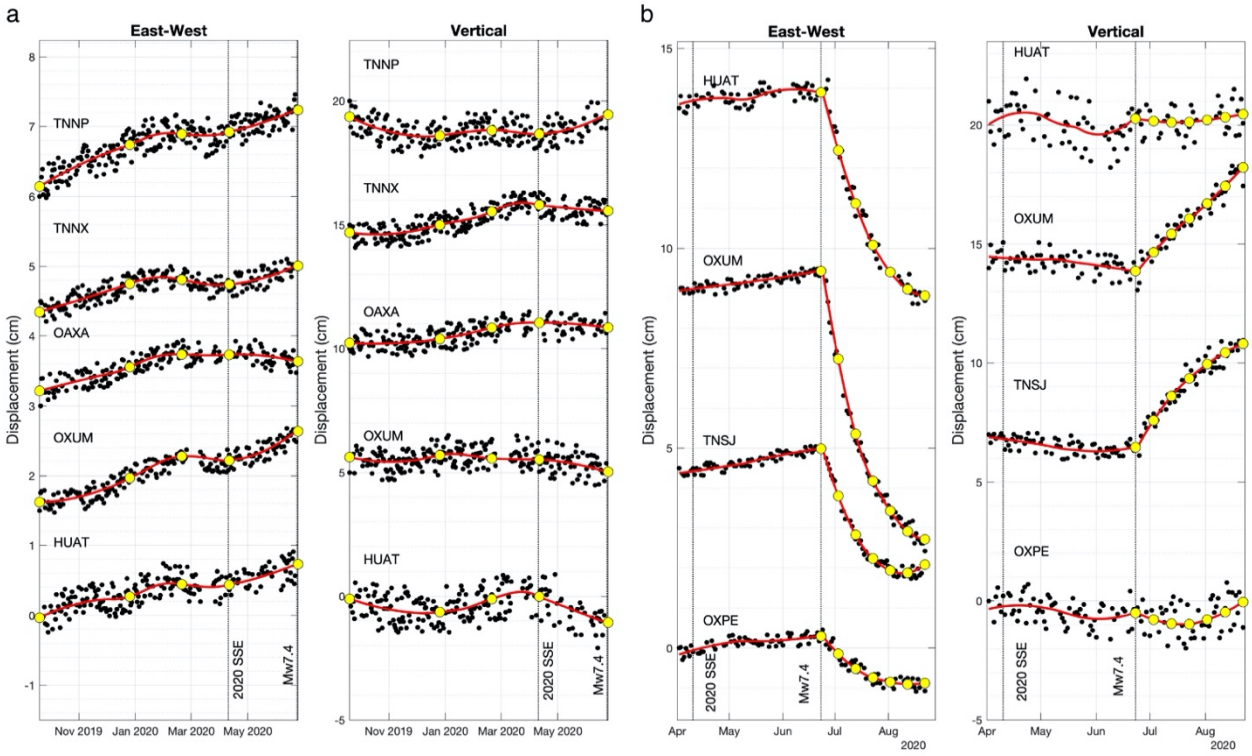

Figure S10 East-west and vertical GNSS displacement time series estimated with the Gipsy-Oasis software for the pre-seismic (a) and post-seismic (b) periods in selected stations shown in Figures 2 and 3.

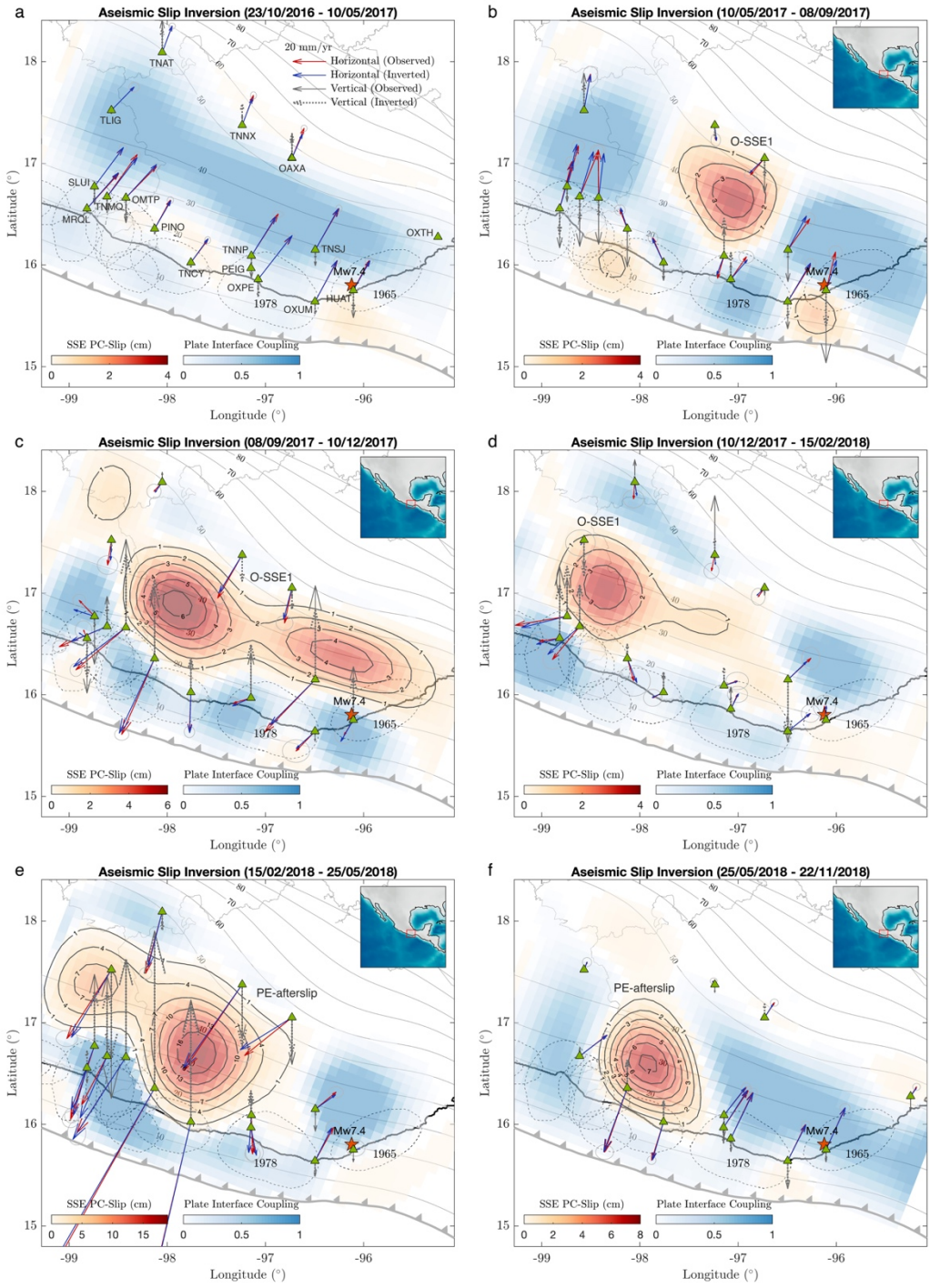
a
Aseismic Slip Inversion (23/10/2016 - 10/05/2017)
b
Aseismic Slip Inversion (10/05/2017 - 08/09/2017)
c
Aseismic Slip Inversion (08/09/2017 - 10/12/2017)
d
Aseismic Slip Inversion (10/12/2017 - 15/02/2018)
e
Aseismic Slip Inversion (15/02/2018 - 25/05/2018)
f
Aseismic Slip Inversion (25/05/2018 - 22/11/2018)
20 mm/yr
Horizontal (Observed)
Horizontal (Inverted)
Vertical (Observed)
Vertical (Inverted)
TNAT
TLIG
TNNX
OAXA
SLUI
TNMQ
OMTP
MRQL
PINO
TNNP
TNSJ
OXTH
TNCY
PEIG
OXPE
OXUM
HUAT
Mw7.4
1978
1965
O-SSE1
PE-afterslip
SSE PC-Slip (cm)
Plate Interface Coupling
Latitude (°)
Longitude (°)

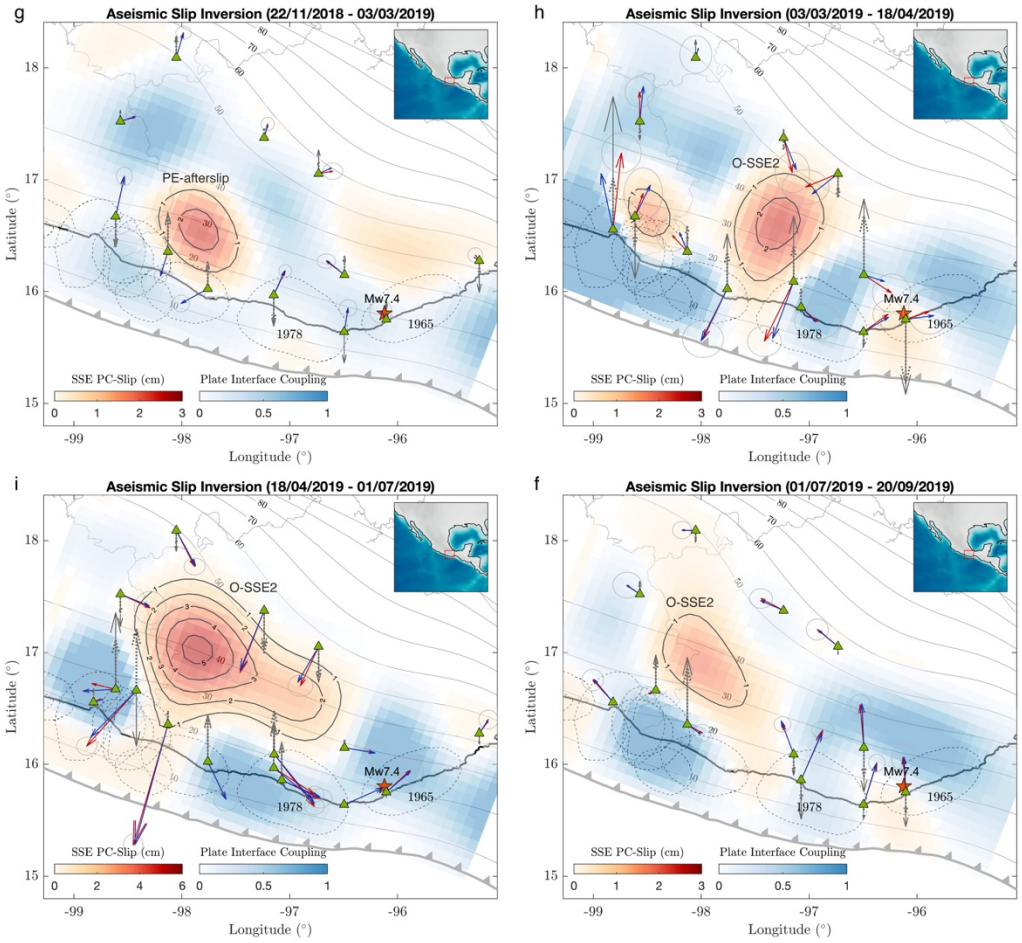

Figure 11 Detailed evolution aseismic slip inversions in Oaxaca from October 2016 to September 2019 including the 2017 Oaxaca SSE (O-SSE1), the Pinotepa earthquake afterslip (PE-afterslip) and the 2019 Oaxaca SSE (O-SSE2)(see also Supplementary Movie S1).

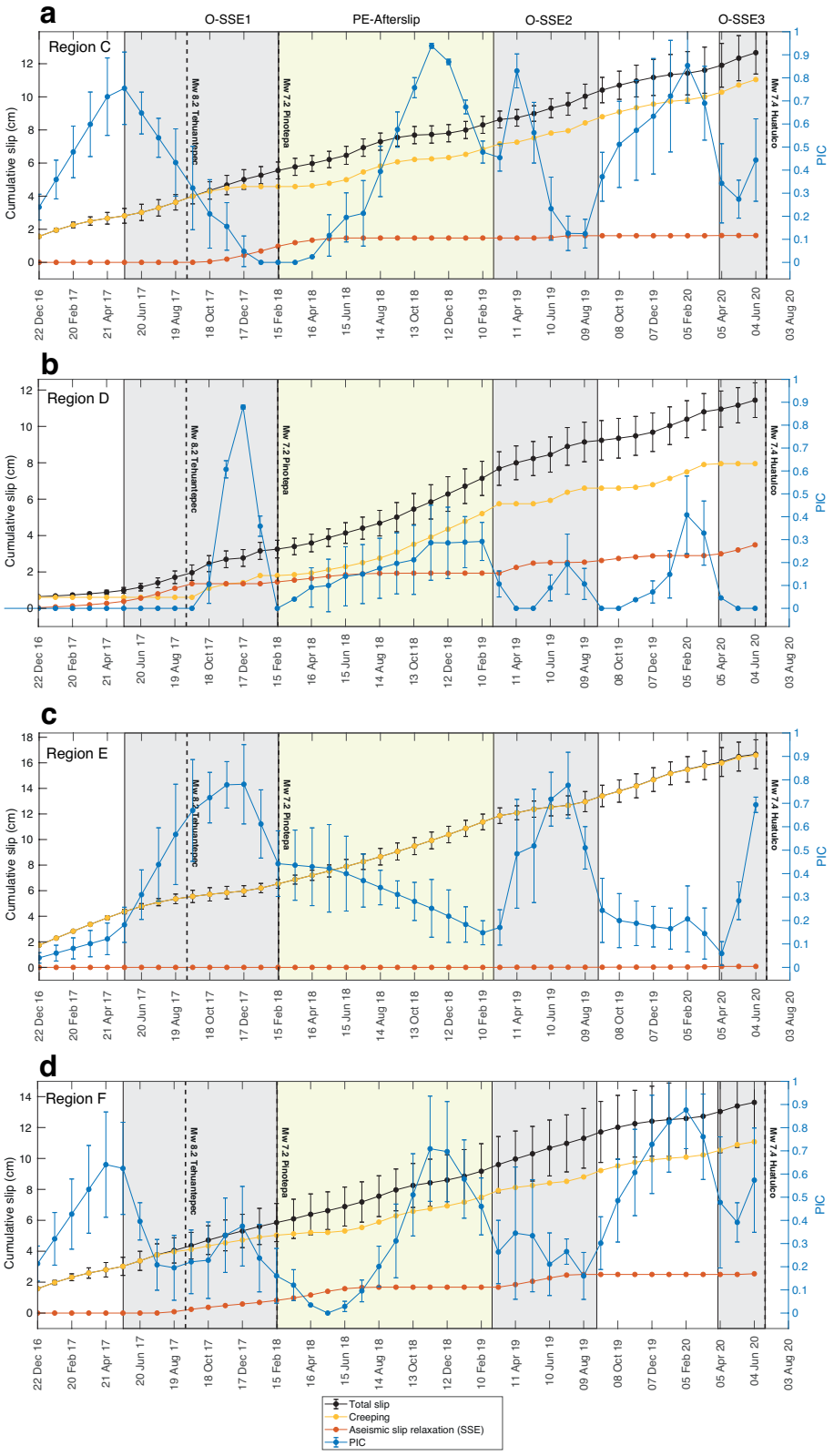

Figure S12 Evolution of the cumulative total slip, creeping (slip under coupling regime), relaxing aseismic slip (SSEs and afterslip) and plate interface coupling (PIC) in regions C, D, E and F (see Figure 4).

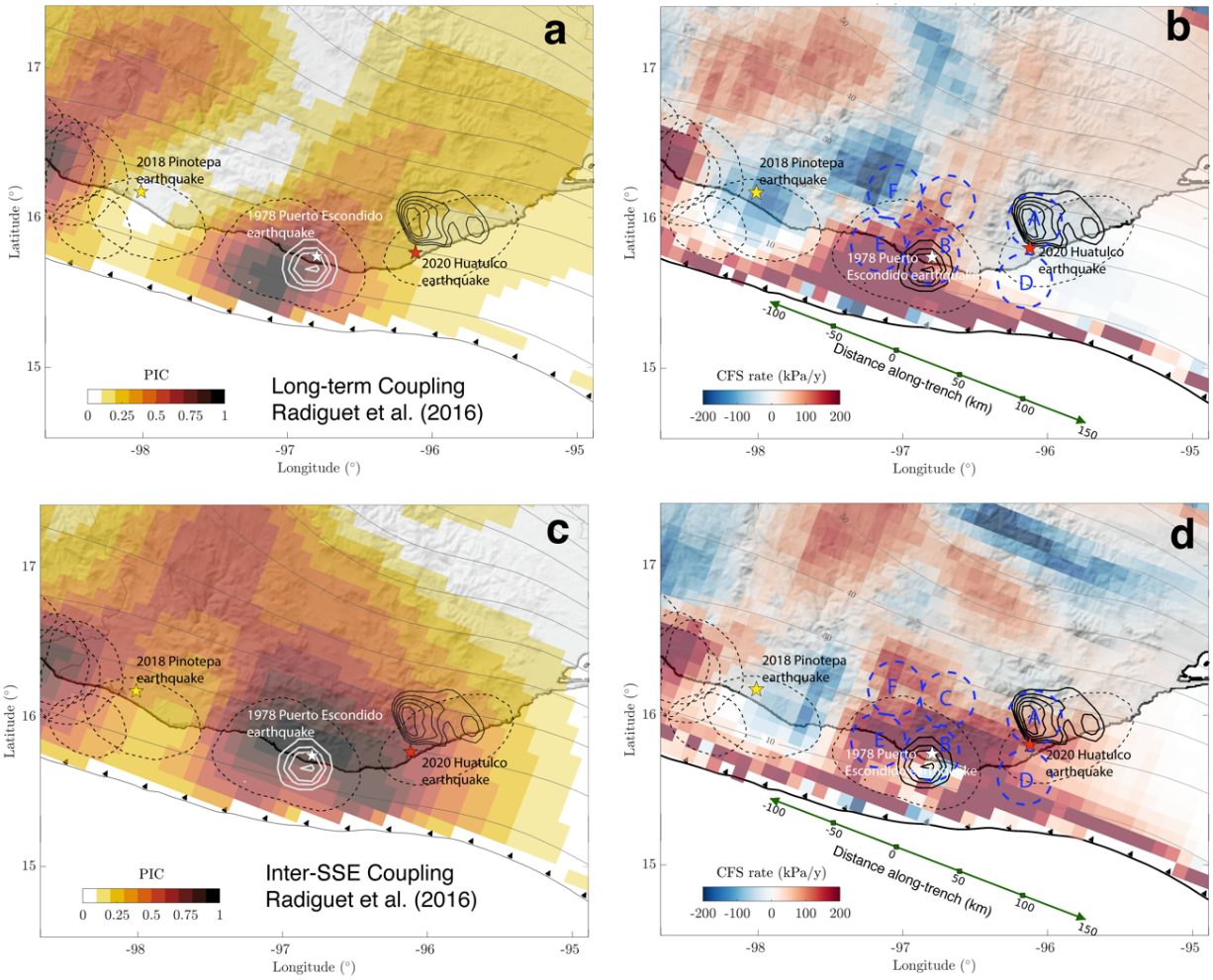

Figure S13 Long-term and inter-SSE time-invariant interplate coupling models estimated by Radiguet et al. (2016) for the Oaxaca subduction zone and their associated CFS rates.

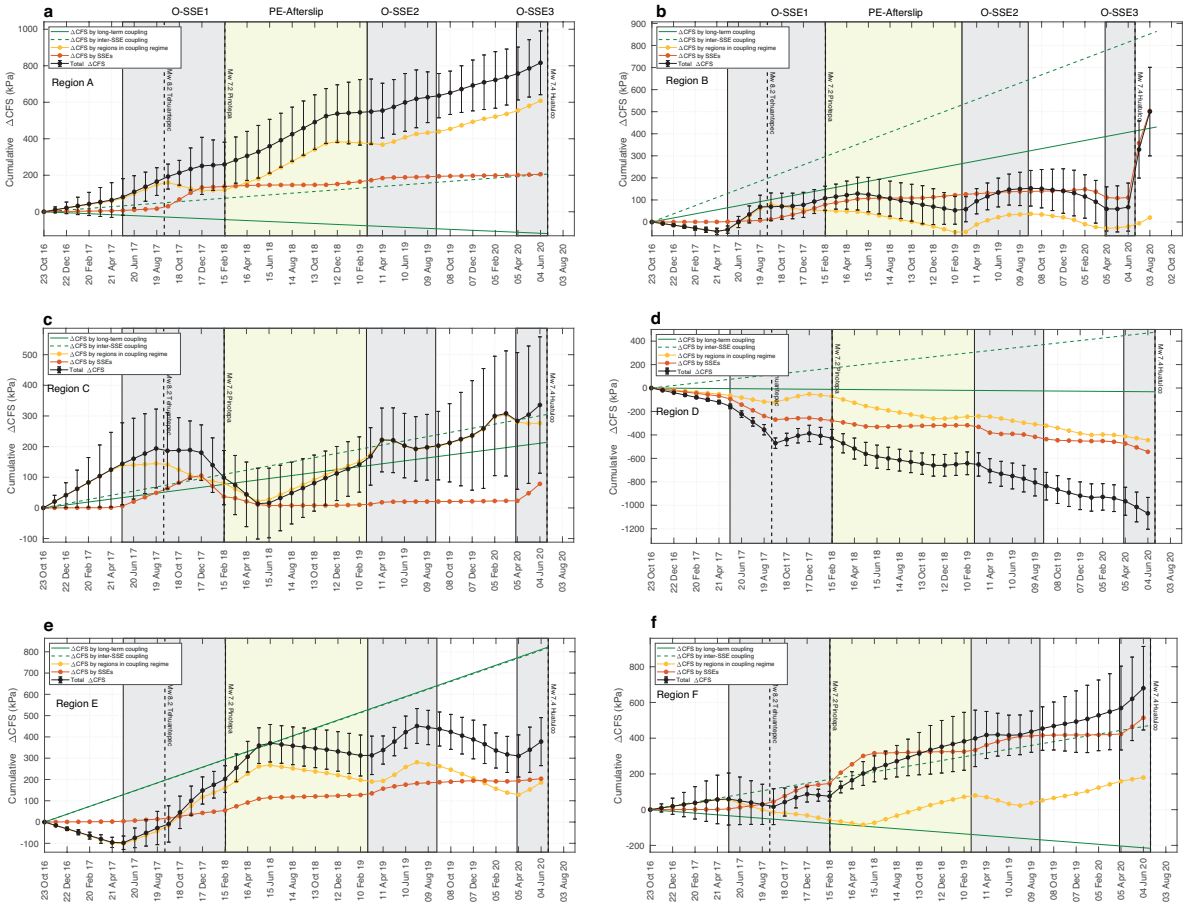

Figure S14 Evolution of the stress partitioning in the seismogenic zone in Oaxaca. Every panel show the evolution of the total CFS (black curves) and their contributions from the relaxing aseismic slip (red curve) and coupled regions (yellow curve), for Regions A-F. Gray rectangles indicate the occurrence of SSEs in the region. The light-yellow rectangle shows the period when the postseismic afterslip of the 2018 Pinotepa and 2020 Huatulco earthquakes developed in the region.

Additional Supporting Information (Files uploaded separately)

Caption of Movie S1. Evolution of the aseismic slip and the CFS in Oaxaca from May 2017 to August 2020 including the pre-seismic and postseismic phases of the 2020 Huatulco earthquake. Left panel show the aseismic slip rate evolution for the relaxing slip (in cm/yr) and the plate interface coupling (PIC) interpolated every 30 days. Right panel shows the accumulated CFS (in kPa) during 30 days prior to the date indicated in the upper part of the panel. Please notice the change of the colorbar scale in both aseismic slip rate and CFS after the occurrence of the 2020 Huatulco earthquake.

Supplementary References

Bevis, M., Brown, A. Trajectory models and reference frames for crustal motion geodesy. *J Geod* **88,** 283–311 (2014). https://doi.org/10.1007/s00190-013-0685-5.

Chen, C. W., & Zebker, H. A. (2000). Network approaches to two-dimensional phase unwrapping: intractability and two new algorithms. *JOSA A*, *17*(3), 401–414.

Cruz-Atienza, V.M., Tago, J., Villafuerte, C., Wei, M., Garza-Girón, R., Dominguez, L.A., Kostoglodov, V., Nishimura, T., Franco, S., Real, J., 2021. Short-Term Interaction between Silent and Devastating Earthquakes in Mexico. Nature Communications, DOI : 10.1038/s41467-021-22326-6.

DeMets, C., Gordon, R.G., Argus, D.F., 2010. Geologically current plate motions. Geophysical Journal International 181, 1-80.

Farr, T. G., Rosen, P. A., Caro, E., Crippen, R., Duren, R., Hensley, S., … Alsdorf, D. E. (2007). The shuttle radar topography mission. *Reviews of Geophysics*, *45*(2), 1–43.

Goldstein, R. M., & Werner, C. L. (1998). Radar interferogram filtering for geophysical applications. *Geophysical Research Letters*, *25*(21), 4035–4038. https://doi.org/10.1029/1998GL900033

Hanssen, R. F. (2001). *Radar interferometry: data interpretation and error analysis* (Vol. 2).

Springer Science & Business Media.

Heki K (2001) Seasonal modulation of interseismic strain buildup in Northeastern Japan driven by snow loads. Science 293:89–92.

Lagler, K., Schindelegger, M., Böhm, J., Krásná, H., Nilsson, T., 2013. GPT2: Empirical slant delay model for radio space geodetic techniques. Geophys Res Lett 40, 1069-1073.

Nikkhoo, M., Walter, T.R., 2015. Triangular dislocation: an analytical, artefact-free solution. Geophysical Journal International 201, 1119-1141.

Radiguet, M., Perfettini, H., Cotte, N., Gualandi, A., Valette, B., Kostoglodov, V., Lhomme, T., Walpersdorf, A., Cabral Cano, E., Campillo, M., 2016. Triggering of the 2014 Mw7.3 Papanoa earthquake by a slow slip event in Guerrero, Mexico. Nature Geoscience 9, 829-833.

Rosen, P. A., Gurrola, E., Sacco, G. F., & Zebker, H. (2012). The InSAR scientific computing environment. *Synthetic Aperture Radar, 2012. EUSAR. 9th European Conference On*, 730–733.

Savage, J.C., 1983. A dislocation model of strain accumulation and release at a subduction zone. Journal of Geophysical Research: Solid Earth 88, 4984-4996.

Tago, J., Cruz-Atienza, V.M., Villafuerte, C., Nishimura, T., Kostoglodov, V., Real, J., Ito, Y., 2020. Adjoint Slip Inversion under a Constrained Optimization Framework: Revisiting the 2006 Guerrero Slow Slip Event. Accepted at Geophysical Journal International.

Wang, R., Schurr, B., Milkereit, C., Shao, Z., Jin, M., 2011. An Improved Automatic Scheme for Empirical Baseline Correction of Digital Strong-Motion Records. Bulletin of the Seismological Society of America 101, 2029-2044.